Adaptive land classification and new class generation by unsupervised double-stage learning in Poincare sphere space for polarimetric synthetic aperture radars

doi: 10.1016/j.neucom.2016.11.072

Adaptive land classification and new class generation by unsupervised double-stage learning in Poincare sphere space for polarimetric synthetic aperture radars

Yuto Takizawa[a], Fang Shang[b], Akira Hirose[a]

[a]*Department of Electrical Engineering and Information Systems, The University of Tokyo, 7-3-1 Hongo, Bunkyo-ku, Tokyo 113-8656, Japan*
[b]*Department of Communications Engineering and Informatics, University of Electro-Communications, 1-5-1, Chofugaoka, Chofu, Tokyo, 182-8585, Japan*

Abstract

Polarimetric satellite-borne synthetic aperture radar (PolSAR) is expected to provide land usage information globally and precisely. In this paper, we propose a unsupervised double-stage learning land state classification system using a self-organizing map (SOM) that utilizes ensemble variation vectors. We find that the Poincare sphere parameters representing the polarization state of scattered wave have specific features of the land state, in particular, in their ensemble variation rather than spatial variation. Experiments demonstrate that the proposed PolSAR double-stage SOM system generate new classes appropriately, resulting in successful fine land classification and/or appropriate new class generation.

Keywords:
Synthetic aperture radar, polarimetry, self-organizing map, geoscience big data

1. Introduction

Satellite-borne synthetic aperture radar (SAR) systems observe the earth continuously, globally and precisely for various purposes [1, 2, 3, 4, 5, 6, 7, 8, 9, 10, 11, 12] such as monitoring and mitigation of disaster [13, 14], forest biomass estimation for CO_2 reduction, glacier movement watching for water resource protection [15] as well as agricultural crop estimation in the near future. They are also expected to observe various natural and artificial land states. For such purposes, polarimetric SAR (PolSAR) will play an important role in newly launched and future satellite systems[16, 17, 18, 19, 20, 21, 22, 23]. In 1990s, some researchers

proposed the use of neural networks in PolSAR classification [18]. However, in these years in this field, most of papers deal with decomposition of so-called coherency / correlation matrix, which is the method closest to practical use in present PolSAR automatic land use classification [24, 25]. Its basis lies in the linear algebra. However, it sometimes fails in meaningful classification because of its non-uniqueness in the decomposition solution.

Instead of matrix decomposition, we previously proposed the use of Sotokes parameters (or Poincare sphere parameters) as the primary variables in the land classification [26]. We also constructed an adaptive classification system based on supervised learning in quaternion domain [27]. With the Stokes representation, the neural classification performance is so high and the learning cost is so light that its practical application is strongly expected.

Though the supervised learning system shows a high accuracy in its adaptive classification, it does not have the ability to discover new categories of land use. Instead, it indicates uncategorized areas as an undetermined class. Unsupervised learning system may have the ability to discover new classes adaptively. For example, self-organizing map (SOM) with a large number of neurons will generate new classes at appropriate position in the SOM feature space.

In this paper, we propose an unsupervised adaptive method to classify land states using a high-dimensional Poincare-sphere-space self-organizing map that deals with ensemble variation of scattering polarization features. It is a type of quaternion neural networks [28, 29, 30], an extended version of complex-valued neural networks (CSOM) [31, 32, 33, 34, 35, 36] so that it deals with rotation and amplification/attenuation in three-dimensional feature space of Poincare sphere. In the present case, however, the SOM dynamics include only addition and subtraction without spinor multiplication. Then the basic processing is similar to real-valued high-dimensional SOM. Previously, we reported a preliminary results [37]. In this paper, we newly show its two advantages. One is the auto-generation of new classes. The other is a high spatial resolution revealed with small targets. The latter merit is also compared with supervised learning results.

In the proposal, we employ double-stage clustering to utilize the dispersion features, or ensemble variation features, of pre-grouped polarization clusters. In this method, first we extract the scattering feature values as Poincare sphere parameters. Then, we group the pixel parameters locally and finely into clusters. Secondly, we classify the clusters adaptively by using a SOM by taking the ensemble variation of respective clusters into consideration. The preliminary grouping also realizes high robustness against the slant-angle changes in the radar observation to yield useful ensemble variation of the Poincare sphere parameters. It

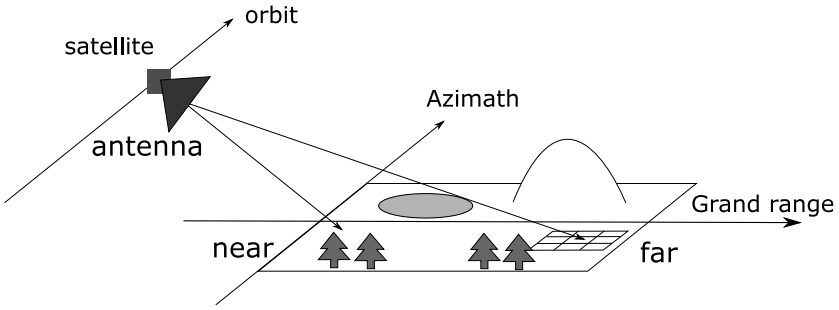

Figure 1: Satellite-borne SAR observation system and the changes of incidence angles.

also realizes a high spatial resolution in comparison with the conventional spatial-variation methods.

Experiments to deal with L-band PALSAR 1.1 level data of Advanced Land Observation Satellite (ALOS), Japan Aerospace Exploration Agency (JAXA), demonstrates that the proposed system generates new classes appropriately to represent finer land classification as well as to discover new object classes. These functions will be highly useful in the big-data geoscience era.

2. Poincare sphere parameters: Position vector and variation vector

Fig. 1 shows the observation geometry in a satellite-borne synthetic aperture radar system. It employs the so-called side-looking observation. Full PolSAR system observes 2×2 complex scattering matrix $\mathbf{S}$ at each resolution area. The calculation of Poincare sphere parameters requires to suppose a certain incident wave. The incident wave is expressed by a unit Jones vector $[E_{\mathrm{H}}^{\mathrm{i}} \quad E_{\mathrm{V}}^{\mathrm{i}}]^T$ where $(\cdot)^T$ denotes transpose and H, V and i stand for horizontal/vertical polarization and incident wave.

The Jones vector of scattered and received wave $[E_{\mathrm{H}}^{\mathrm{r}} \quad E_{\mathrm{V}}^{\mathrm{r}}]^T$ is obtained as

$$\begin{bmatrix} E_{\mathrm{H}}^{\mathrm{r}} \\ E_{\mathrm{V}}^{\mathrm{r}} \end{bmatrix} = \begin{bmatrix} S_{\mathrm{HH}} & S_{\mathrm{HV}} \\ S_{\mathrm{VH}} & S_{\mathrm{VV}} \end{bmatrix} \begin{bmatrix} E_{\mathrm{H}}^{\mathrm{i}} \\ E_{\mathrm{V}}^{\mathrm{i}} \end{bmatrix} \tag{1}$$

where $E_{\mathrm{H}}^{\mathrm{r}}$ and $E_{\mathrm{V}}^{\mathrm{r}}$ stand for horizontal and vertical polarization components, respectively. The averaged Stokes vector $[\langle g_0 \rangle \ \langle g_1 \rangle \ \langle g_2 \rangle \ \langle g_3 \rangle]^T$ is then obtained as

$$\begin{bmatrix} \langle g_0 \rangle \\ \langle g_1 \rangle \\ \langle g_2 \rangle \\ \langle g_3 \rangle \end{bmatrix} = \begin{bmatrix} \langle E_H^{\mathrm{r}} E_H^{\mathrm{r}*} \rangle + \langle E_V^{\mathrm{r}} E_V^{\mathrm{r}*} \rangle \\ \langle E_H^{\mathrm{r}} E_H^{\mathrm{r}*} \rangle - \langle E_V^{\mathrm{r}} E_V^{\mathrm{r}*} \rangle \\ \langle E_H^{\mathrm{r}} E_V^{\mathrm{r}*} \rangle + \langle E_V^{\mathrm{r}} E_H^{\mathrm{r}*} \rangle \\ j(\langle E_H^{\mathrm{r}} E_V^{\mathrm{r}*} \rangle - \langle E_V^{\mathrm{r}} E_H^{\mathrm{r}*} \rangle) \end{bmatrix} \tag{2}$$

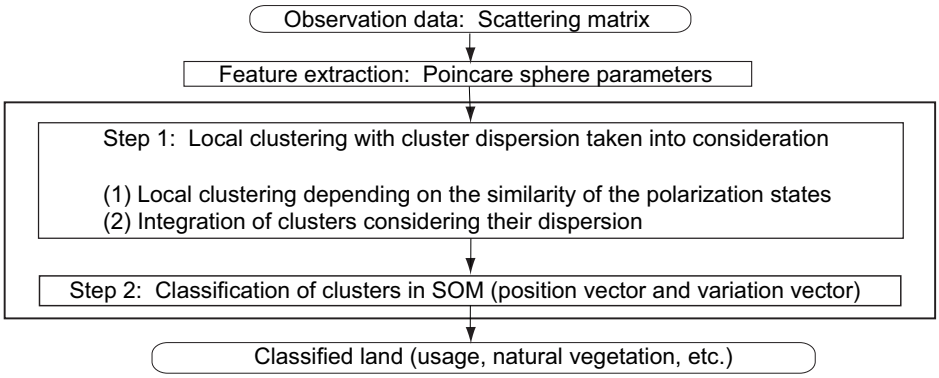

Figure 2: Total processing flow of the proposed adaptive land state classification system using a SOM in the double-stage learning.

where $\langle\cdot\rangle$ denotes spatial or other averaging process and $(\cdot)^*$ means complex conjugate. We define a variable on/in the Poincare sphere $\boldsymbol{P}$ representing polarization states in three dimension as

$$\boldsymbol{P} = \left(\frac{\langle g_1 \rangle}{\langle g_0 \rangle}, \frac{\langle g_2 \rangle}{\langle g_0 \rangle}, \frac{\langle g_3 \rangle}{\langle g_0 \rangle} \right) \equiv (x, y, z) \tag{3}$$

We name $\boldsymbol{P}$ the position vector that represent the position in Poincare space. The norm of $\boldsymbol{P}$ gives the degree of polarization (DoP) as

$$\mathrm{DoP} = \sqrt{\langle g_1 \rangle^2 + \langle g_2 \rangle^2 + \langle g_3 \rangle^2} / \langle g_0 \rangle \tag{4}$$

The position vector $\boldsymbol{P}$ is a three dimensional vector relevant to the polarization states of the incident wave. If we consider $\boldsymbol{P}$ for all the possible incident polarization states, the computational cost will be huge. Instead, we use only important four polarization states, $\boldsymbol{P}_{\mathrm{H}}$, $\boldsymbol{P}_{\mathrm{V}}$, $\boldsymbol{P}_{45^\circ}$ and $\boldsymbol{P}_{\mathrm{lc}}$, namely, horizontal, vertical, 45° and left-handed circular polarization [26], as the incident polarization in the following experiments.

3. Adaptive classification by unsupervised double-stage learning

3.1. Overall processing flow

The total process is composed of local clustering in strict condition and unsupervised learning classification of the clusters. Fig. 2 shows the processing flow in total. A rough description is given here first and then, followed by detailed explanation in the next subsections. In this proposal, Step 1 is local clustering to

realize the utilization of the variation of Poincare sphere parameters in respective land state clusters in the following process. By regarding a set of position vectors $\boldsymbol{Q} = [\boldsymbol{P}_H^T\ \boldsymbol{P}_{lc}^T\ \boldsymbol{P}_{45^\circ}^T\ \boldsymbol{P}_V^T]^T$ as the input vector representing features of each pixel, we conduct the clustering in Step 1 by considering the dispersion of the clusters under construction. We also implement strict clustering with the condition using the dispersion of local clusters.

This local clustering also mitigates the distortion in the radar observation because of the strict condition of local clustering and the order of scanning. As illustrated in Fig. 1, a satellite-borne SAR transmits electromagnetic-wave to the earth surface with a slant angle. Hence, the scattered-wave polarization depends on the incident angle [20]. That is, similar land states located near or far range results in polarization states different from one another. This problem mainly arises in the grand range direction. This concern happens also depending on the terrain shape such as slopes and mountains. Therefore, in Step 1 local clustering, we first scan in the azimuth direction, and then proceed line by line in the range direction. Because of this order of scanning and the strict condition of clustering, the pixels far from each other seldom belong to a single cluster, resulting in fine local clusters. Then, we calculate the mean value $\boldsymbol{Q}(i)$ and the standard deviation $\boldsymbol{s}(i)$ for i-th cluster data.

In Step 2, we classify the clusters adaptively by using SOM. Each cluster has a 24-dimensional feature vector. We found in the following experiments that, even when two areas are located away from each other, common features exist in their parameter distributions corresponding to land states especially in the ensemble variation. Hence, in this process, we multiply the variation by an appropriate weight in order to emphasize its contribution. We describe the details in Section 3.3.

3.2. Local clustering

Step 1 includes the following two processes, i.e. local clustering depending on the similarity of the polarization states and integration of clusters considering their variation.

(1) Local clustering depending on the similarity of the polarization states:
We examine the distances between the scanning center pixel's input vector $\boldsymbol{Q}^c$ and its surrounding eight pixel vectors $\boldsymbol{Q}^s$. We consider the difference of polarization states of scattered waves as sum of the euclidean distances in the four incidence Poincare sphere parameters to calculate distance $D(\boldsymbol{Q}^c, \boldsymbol{Q}^s)$ as

$$D(\boldsymbol{Q}^c, \boldsymbol{Q}^s) = \ \|\boldsymbol{P}_{\mathrm{H}}^c - \boldsymbol{P}_{\mathrm{H}}^s\| + \|\boldsymbol{P}_{\mathrm{V}}^c - \boldsymbol{P}_{\mathrm{V}}^s\| + \|\boldsymbol{P}_{45^\circ}^c - \boldsymbol{P}_{45^\circ}^s\| + \|\boldsymbol{P}_{\mathrm{lc}}^c - \boldsymbol{P}_{\mathrm{lc}}^s\| \quad (5)$$

If $D(\boldsymbol{Q}^c, \boldsymbol{Q}^s)$ is less than a strict threshold $D_{\rm th}$, which is properly set based on the clustering fitness as explained in Section 4.1, we regard pixels c and s in a single land state cluster.
(2) Integration of clusters considering their variation:
If the input vector of a new pixel labeled a new label is close sufficiently to an existing cluster's mean value $\boldsymbol{Q}(i)$, the pixel is integrated into the cluster at this time by the process described in the next paragraph. However, in the case that the input vector is away from the center of the existing cluster by the standard deviation or more, it sometimes happens that a cluster j whose land state is actually the same as that of an existing cluster k is generated because of the strict condition.

We integrate them in the every azimuth direction line scanning, namely after the new pixel make a cluster with enough number of pixels and the mean value $\boldsymbol{Q}(j)$ with them. We use $n(j)$ to represent the number of pixels in cluster j. When $n(j)$ is less than $n(k)$ and the following condition F is fulfilled, we integrate cluster j and cluster k. The condition F is determined based on the standard deviation $u\boldsymbol{s}(k)$ where u is a scale. In this process, we change u decreasingly from u_s to u_e according to the increase of $n(k)$ which is a parameter deciding the decreasing speed. That is, we integrate clusters j and k when all the elements of $\boldsymbol{Q}_{\rm Element}(j)$ are within a distance determined by the standard deviation $u\boldsymbol{s}(k)$ from $\boldsymbol{Q}_{\rm Element}(k)$:

$$F(j,k,u) : |\boldsymbol{Q}_{\rm Element}(j) - \boldsymbol{Q}_{\rm Element}(k)| < u\boldsymbol{s}_{\rm Element}(k)\ (^{\forall}{\rm Element}) \tag{6}$$

$$u = u_e + \frac{u_s - u_e}{1 + n(k)/N} \tag{7}$$

where N is a constant determining the decreasing speed. When a new label is made by a new pixel, it is conducted as $\boldsymbol{Q}_{\rm Element}(j) = \boldsymbol{Q}^c$ and $n(j) = 1$ in stricter condition with $F'(j,k,u')$ and $u'(u'_s, u'_e)$. The details are given in Section 4.1. With these processes, we can conduct the strict clustering based on the dispersion of Poincare sphere parameters, which is robust against the angle changes of the side-looking satellite observation.

3.3. Adaptive classification by SOM

We define the feature vector of i-th clusters as a combination of a set of the position vectors $\boldsymbol{Q}(i)$ and a set of the variation vectors (standard deviation vectors) $\boldsymbol{s}(i)$, that is,

$$\boldsymbol{T}(i) = \begin{bmatrix} \boldsymbol{Q}(i) \\ \boldsymbol{s}(i) \end{bmatrix} \tag{8}$$

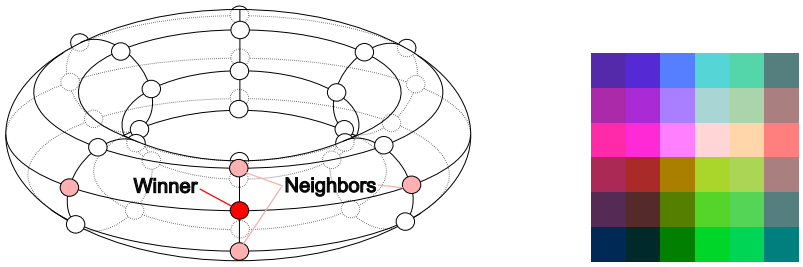

(a) (b)

Figure 3: (a) Torus SOM space and (b) the neuron-label color map.

We use a SOM to classify the clusters suitably based on the feature vectors just like we do in our ground penetrating radar (GPR) systems [36, 38, 39]. In the present SAR classification system, we choose a 6×6 torus as neuron topology.

Then the input signal is a 24-dimensional feature vector for a cluster $\boldsymbol{T}^{\boldsymbol{in}}(i)$. We associate neuron g with a weight vector $\boldsymbol{T}^{\boldsymbol{w}}(g)$ having the same dimension as that of the input signal. We classify an i-th input into a class represented by a neuron g when the the following distance becomes minimum for g among neuron classes:

$$H(\boldsymbol{T}^{\boldsymbol{in}}(i), \boldsymbol{T}^{\boldsymbol{w}}(g)) = D(\boldsymbol{Q}(i), \boldsymbol{Q}^{\boldsymbol{w}}(g)) + KD(\boldsymbol{s}^{\boldsymbol{in}}(i), \boldsymbol{s}^{\boldsymbol{w}}(g)) \tag{9}$$

where we put an emphasis on the dispersion information in such a way that we first normalize $\boldsymbol{Q}(i)$ and $\boldsymbol{s}(i)$, and then multiply normalized $\boldsymbol{s}(i)$ with an appropriate weight K_0 (i.e., $K = K_0\sigma(\boldsymbol{Q}(i))/\sigma(\boldsymbol{s}(i))$). We set the weight K_0 empirically by minimizing the classification error. Self-organization occurs as the updates of the winner $\boldsymbol{T}^{\boldsymbol{w}}_{\mathrm{win}}(g)$ and the surrounding neurons $\boldsymbol{T}^{\boldsymbol{w}}_{\mathrm{neighbor}}(g)$ with the sequential signal input. We input the features of $i = 1$st cluster to $i = I$-th cluster. Then we repeat this process for a sufficient C times. We determine empirically the self-organization coefficients α_0 and β_0 properly to use them varying with the iteration number c as

$$\begin{aligned} \boldsymbol{T}^{\boldsymbol{w}}_{\mathrm{win}}(t+1) =& \boldsymbol{T}^{\boldsymbol{w}}_{\mathrm{win}}(t) + \alpha(\boldsymbol{T}^{\boldsymbol{in}} - \boldsymbol{T}^{\boldsymbol{w}}_{\mathrm{win}}), \quad \alpha = \alpha_0(1 - c/C), \\ \boldsymbol{T}^{\boldsymbol{w}}_{\mathrm{neighbor}}(t+1) =& \boldsymbol{T}^{\boldsymbol{w}}_{\mathrm{neighbor}}(t) + \beta(\boldsymbol{T}^{\boldsymbol{in}} - \boldsymbol{T}^{\boldsymbol{w}}_{\mathrm{neighbor}}), \quad \beta = \beta_0(1 - c/C). \end{aligned} \tag{10}$$

4. Experiments and results

4.1. Observation data and double-stage SOM setup

The observation data used in the following experiment is L-band PALSAR 1.1 level data of ALOS, JAXA, observing the Mt. Fuji area having 2932×1048

pixels. This data is so large and contains much enough kinds of land states in an experiment. We set N=1,000. The spatial averaging process in (2) is calculated for 5×5 local window.

Fig. 3(a) shows the SOM space structure. It is two-dimensional in torus. We employ a rectangle network so that a winner neuron has four neighbor neurons. Fig. 3(b) presents the 6×6 color map corresponding to the above 36 neurons. The color was assigned in such a way that, if two neurons are neighbors to each other, the colors (hue and saturation) are near. Then we can interpret SOM classification results intuitively by looking at the color classification map.

We determined the constants and coefficients introduced in the above process empirically at best values in a series of experiments. Since the distance of each position vectors in a single class is about 0.2 in average, we determined $D_{\rm th}$=0.8 ($= 0.2 \times 4$). We also determined u_s=3, u_e=2, u'_s=2 and u'_e=1 and set the maximum and the minimum of the condition F as $F_{\rm min}$=0.3 and $F_{\rm max}$=0.5, while F' as $F'_{\rm min}$=0.1 and $F'_{\rm max}$=0.2, by analyzing quantitatively the position vectors. Step 1 generates about 400 clusters whose populations are $1-$200,000. Then, in Step 2, the SOM classifies the clusters with K_0=10.0, a_0=0.3, b_0=0.04 and C=200.

4.2. Land classification results

Fig. 4 shows the results of various unsupervised classification methods. Fig. 4(a) is the result of SOM using only position vectors $\boldsymbol{Q}(i)$ while (b) is the result using $\boldsymbol{Q}(i)$ and the spatial variation as we did in Ref. [27], and (c) is the result of the proposal using $\boldsymbol{T}(i)$, i.e., position vectors $\boldsymbol{Q}(i)$ and ensemble variation $\boldsymbol{s}(i)$ as (8). The class colors are synchronized among them in such a manner that the lakes show the same light blue. Fig. 4(d) is a Google photo of the observation area with a transform into the same aspect ratio, and (e) is a sketch presenting rough four classes shown in Ref. [27].

Table 1 shows quantitatively the coincidence comparison calculated for 5000 pixels in lake, grass, forest and city areas, respectively. Here, coincidence stands for accuracy in the case of supervised learning. Fig. 4(d) shows the numerical evaluation areas of the four land states by white squares. We find that the proposed method achieves the highest overall coincidence. We analyze the details below.

The result using only the position vector in Fig. 4(a) shows a good classification for the lakes, though the lake centers are classified wrongly. This error is attributed to the insensitiveness of Poincare parameters (position vectors and variation vectors) to the wave amplitude because of the normalization in the Stokes vector calculation and the high number (36) of the possible classes. Besides, the

Table 1: Unsupervised classification coincidence for the Fujisusono area.

Utilizing	State	Coincidence	Overall Coincidence
(a) No dispersion information	Lake	99.32%	37.33%
	Grass	0% (96.92% as Lake)	
	Forest	5.06%	
	Town	41.86%	
(b) Spatial fluctuation	Lake	97.88%	51.50%
	Grass	64.36%	
	Forest	8.98%	
	Town	34.78%	
(c) Variance in the local clusters	Lake	93.60%	83.24%
	Grass	74.72%	
	Forest	86.60%	
	Town	78.02%	

large grass area near the big lake is classified to the lake class. The most serious problem is that the large forest area is classified to various classes. The color distributes widely in the SOM space, showing less meaningful classification. In Fig. 4(b) using spatial variation vector, the classification trend is very similar to (a), though the spatial resolution is apparently lower. However, in the result of proposed method shown in Fig. 4(c), the result is different. The 36 classes are composed of about 7 main classes and other exceptional classes including only a few pixels. The forest areas are classified stably. Town areas include several classes, but are segmented clearly from the forest areas. The results demonstrate that the double-stage SOM method classifies the polarimetric image adaptively and stably by using the ensemble variation vectors as well as the position vectors.

Fig. 5 plots the position vectors for horizontal, 45° linear, left circular and vertical polarizations corresponding to the major five classes in the result of the proposed method in Fig. 4(c). The position vectors clearly present distributions different from one another depending on the land states. This fact suggests that the proposed method has the ability to classify the land use adaptively.

4.3. Generation of new classes

The main advantages of the proposed method lie in its ability of new-class generation and high-resolution classification. Fig. 6 compares the proposed SOM unsupervised learning result with the supervised learning result reported in Ref. [27].

Respective images show:

(a) Supervised learning result to classify the data image into four classes, namely, green: forest, light green: grass, blue: lake, and red: town.
(b) Unsupervised learning result to classify the data image into 36 classes in the proposed self-organizing manner, which is identical with Fig. 4(c).
(c) Google photo identical with Fig. 4(d).

(a1) Close-up of a grass area in (a).
(b1) Close-up of a grass area in (b).
(c1) Close-up of a grass area in (c).

(a2) Close-up of a forest area in (a). Note that this area is on a so large hill that foreshortening effect causes a shift of the target location. The arrow indicates the original location.
(b2) Close-up of a forest area in (b). Note that this area is on a so large hill that foreshortening effect causes a shift of the target location. The arrow indicates the original location.
(c2) Close-up of a forest area in (c). No foreshortening effect occurs.

In addition, Fig. 7 is the plots of position vectors for the finer classes appearing in Fig. 7(b1). The distributions for horizontal and vertical incident waves (Fig. 7(a) and (d)) has only a slight dependence on the land state. However, those for 45° and left circular incidence present meaningful dependence. By examining the ground truth, we have found that the classes correspond to grass, grass with sparse trees, soil-dominant grass and water-covering grass. Accordingly, the rough "grass" in the supervised results can be analyzed and divided into finer classes in the unsupervised learning. The spatial distribution of the classes in Fig. 7(b1) is found corresponding to the land states estimable in (c1). It is found that the unsupervised learning realizes a finer classification successfully.

Fig. 7(b2) includes ski gelaende where the trees are felled. The gelaende location is shifted in the foreshortening effect in comparison with that in (c2) Google photo. The cut down area is so thin that it was not detectable by the previous supervised learning using spatial variation where the resolution is low and the class number was fixed at four. Contrarily, the proposed method used the generated new class appropriately for this extraction. This result also demonstrates the merit of the proposal. Accordingly, we find that the proposed method holds the merits of the new-class generation and the high-resolution classification.

5. Conclusion

We proposed the PolSAR double-stage SOM classification that self-organizingly classifies the Poincare sphere parameters consisting of position vectors and their ensemble variation vectors. Experiments dealing with L-band PALSAR 1.1 level data of ALOS, JAXA, demonstrated that the proposed system classifies land use with a high performance. The main advantages lie in the ability of new-class generation and high-resolution classification. It also mitigates the observation-range and terrain influences on the polarization characteristics. This framework will play an important role in the forthcoming big-data geoscience era.

Acknowledgment

A part of this work was supported by JSPS KAKENHI Grant Number 15H02756.

References

[1] D. Ghiglia, M. Pritt, Two-dimensional phase unwrapping: theory, algorithms, and software, Wiley-Interscience publication, Wiley, 1998.

[2] M. Pritt, J. Shipman, Least-squares two-dimensional phase unwrapping using FFT's, IEEE Transactions on Geoscience and Remote Sensing 32 (3) (1994) 706–708.

[3] G. Fornaro, G. Franceschetti, R. Lanari, Interferometric SAR phase unwrapping using Green's formulation, IEEE Transactions on Geoscience and Remote Sensing 34 (3) (1996) 720–727.

[4] P. A. Rosen, S. Hensley, I. R. Joughin, F. K. Li, S. N. Madsen, E. Rodriguez, R. M. Goldstein, Synthetic aperture radar interferometry, Procee 88 (3) (2000) 333–382.

[5] R. M. Goldstein, H. A. Zebker, C. L. Werner, Satellite radar interferometry: Two-dimensional phase unwrapping, Radio Science 23 (1988) 713–720.

[6] A. B. Suksmono, A. Hirose, Adaptive noise reduction of InSAR image based on complex-valued MRF model and its application to phase unwrapping problem, IEEE Transactions on Geoscience and Remote Sensing 40 (3) (2002) 699–709.

[7] R. Yamaki, A. Hirose, Singular unit restoration in interferograms based on complex-valued Markov random field model for phase unwrapping, IEEE Geoscience and Remote Sensing Letters 6 (1) (2009) 18–22.

[8] A. B. Suksmono, A. Hirose, Adaptive noise reduction of InSAR images based on a complex-valued MRF model and its application to phase unwrapping problem, IEEE Transactions on Geoscience and Remote Sensing 40 (3) (2002) 699–709 (followed by publisher's errata on Fig. 12).

[9] J.-S. Lee, W. M. Boerner, D. L. Schuler, T. L. Ainsworth, I. Hajnsek, K. P. Papathanassiou, E. Luneburg, A review of polarimetric SAR algorithms and their applications, Journal of Photogrammetry and Remote Sensing 9 (2004) 31–80.

[10] A. B. Suksmono, A. Hirose, Progressive transform-based phase unwrapping utilizing a recursive structure, IEICE Transactions on Communications E89-B (3) (2006) 929–936.

[11] R. Natsuaki, A. Hirose, SPEC method - a fine co-registration method for SAR interferogram, IEEE Transactions on Geoscience and Remote Sensing 49 (1) (2011) 28–37.

[12] G. Oshiyama, A. Hirose, Distortion reduction in singularity-spreading phase unwrapping with pseudo-continuous spreading and self-clustering active localization, IEEE Journal of Selected Topics in Applied Earth Observations and Remote Sensing 8 (8) (2015) 3846–3858.

[13] M. Shimada, JAXA earth observation program digest, IEEE Geoscience and Remote Sensing Magazine June 2014 (2) (2014) 47–52.

[14] R. Natsuaki, A. Hirose, InSAR local co-registration method assisted by shape-from-shading, IEEE Journal of Selected Topics in Applied Earth Observations and Remote Sensing 6 (2) (2013) 953–959.

[15] N. Usami, A. Muhuri, A. Bhattacharya, A. Hirose, PolSAR wet snow mapping with incidence angle information, IEEE Geoscience and Remote Sensing Letters , to appear.

[16] W. M. Boerner, Recent advances in extra-wide-band polarimetry, interferometry and polarimetric interferometry in synthetic aperture remote sensing

and its applications, IEE Proceedings – Radar, Sonar and Navigation 150 (3) (2003) 113 – 124.

[17] S. R. Cloude, E. Pottier, An entropy based classification scheme for land applications of polarimetric SAR, IEEE Transactions on Geoscience and Remote Sensing 35 (1997) 68–78.

[18] K. S. Chen, W. P. Huang, D. H. Tsay, F. Amar, Classification of multifrequency polarimetric SAR imagery using a dynamic learning neural network, IEEE Transactions of Geoscience and Remote Sensing 34 (1996) 814–820.

[19] R. Touzi, S. Goze, T. Le Toan, A. Lopes, E. Mougin, Polarimetric discriminators for SAR images, IEEE Transactions on Geoscience and Remote Sensing 30 (5) (1992) 973–980.

[20] F. T. Ulaby, D. Held, M. C. Dobson, K. C. McDonald, T. B. A. Senior, Relating polarization phase differencpolarSAR signals to scene properties, IEEE Transactions on Geoscience and Remote Sensing GE-25 (1) (1987) 83 – 92.

[21] D. L. Evans, T. G. Farr, J. J. van Zyl, H. A. Zebker, Radar polarimetry: Analysis tools and applications, IEEE Transactions on Geoscience and Remote Sensing 26 (6) (1988) 774–789.

[22] R. Touzi, R. K. Raney, F. Charbonneau, On the use of permanent symmetric scatterers for ship characterization, IEEE Transactions on Geoscience and Remote Sensing 42 (10) (2004) 2039–2045.

[23] R. Shirvany, M. Chabert, J.-Y. Tourneret, Ship and oil-spill detection using the degree of polarization in linear and hybrid/compact Dual-Pol SAR, IEEE Journal of Selected Topics in Applied Earth Observations and Remote Sensing 5 (3) (2012) 885–892. doi:10.1109/JSTARS.2012.2182760.

[24] Y. Yamaguchi, T. Moriyama, M. Ishido, H. Yamada, Four component scattering model for polarimetric SAR image decomposition, IEEE Transactions on Geoscience and Remote Sensing 43 (8) (2005) 1699–1706.

[25] G. Singh, G. Venkataraman, Y. Yamaguchi, S.-E. Park, Capability assessment of fully polarimetric ALOS-PALSAR data for discriminating wet snow from other scattering types in mountainous regions, IEEE Transactions on Geoscience and Remote Sensing 52 (2) (2014) 1177 – 1196.

[26] F. Shang, A. Hirose, Averaged-Stokes-vector-based polarimetric SAR data interpretation, IEEE Transactions on Geoscience and Remote Sensing 53 (8) (2015) 4536–4547.

[27] F. Shang, A. Hirose, Quaternion neural-network-based PolSAR land classification in Poincare-sphere-parameter space, IEEE Transactions on Geoscience and Remote Sensing 52 (9) (2014) 5693–5703.

[28] N. Matsui, T. Isokawa, H. Kusamichi, F. Peper, H. Nishimura, Quaternion neural network with geometrical operators, Journal of Intelligent and Fuzzy Systems 15 (2004) 149–164.

[29] E. Bayro-Corrochano, Geometric Computing for Wavelet Transforms, Robot Vision, Learning, Control and Action, Springer, 2010.

[30] E. J. Bayro-Corrochano, N. Arana-Daniel, Clifford support vector machines for classification, regression, and recurrence, IEEE Transactions on Neural Networks 21 (11) (2010) 1731–1746.

[31] A. Hirose, S. Yoshida, Generalization characteristics of complex-valued feedforward neural networks in relation to signal coherence, IEEE Transactions on Neural Networks and Learning Systems 23 (2012) 541–551.

[32] T. Hara, A. Hirose, Plastic mine detecting system using complex-valued self-organizing map that deals with multiple-frequency interferometric images, Neural Networks 17 (8-9) (2004) 1201–1210.

[33] S. Masuyama, A. Hirose, Walled LTSA array for rapid, high spatial resolution, and phase sensitive imaging to visualize plastic landmines, IEEE Transactions on Geoscience and Remote Sensing 45 (8) (2007) 2536–2543.

[34] S. Onojima, Y. Arima, A. Hirose, Millimeter-wave security imaging using complex-valued self-organizing map for visualization of moving targets, Neurocomputing 134 (2014) 247–253.

[35] R. Natsuaki, A. Hirose, Circular property of complex-valued correlation learning in CMRF-based filtering for synthetic aperture radar interferometry, Neurocomputing 134 (2014) 165–172.

[36] A. Hirose, Complex-Valued Neural Networks, 2nd Edition, Springer, Heidelberg, Berline, New York, 2012.

[37] Y. Takizawa, F. Shang, A. Hirose, Unsupervised land classification by self-organizing map utilizing the ensemble variance information in satellite-borne polarimetric synthetic aperture radar, in: International Conference on Neural Information Processing (ICONIP) 2015 Istanbul, 2015, pp. 244–252.

[38] S. Masuyama, K. Yasuda, A. Hirose, Multiple mode selection of walled-ltsa array elements for high resolution imaging to visualize antipersonnel plastic landmines, IEEE Geoscience and Remote Sensing Letters 5 (4) (2008) 745–749.

[39] Y. Nakano, A. Hirose, Adaptive identification of landmine class by evaluating the total degree of conformity of ring-SOM, Australian Journal of Intelligent Information Processing Systems 12 (2010) 23–28.

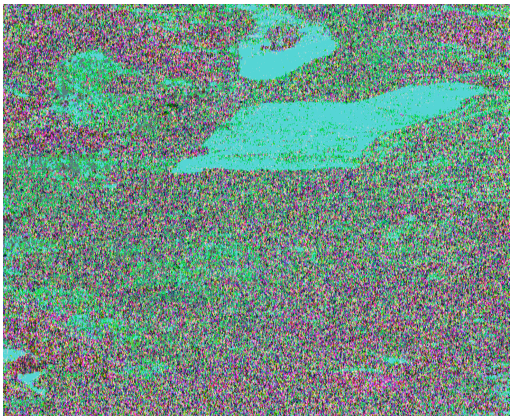

(a)Position vector only

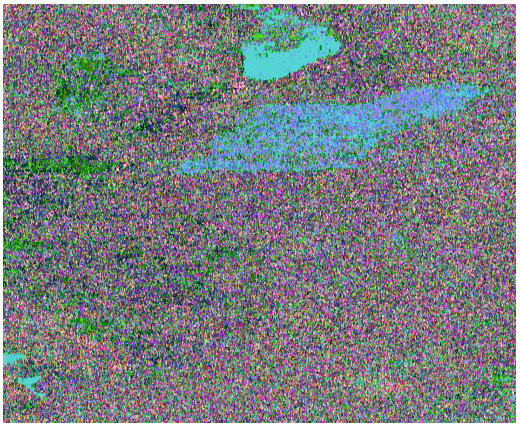

(b)Position and spatial variation

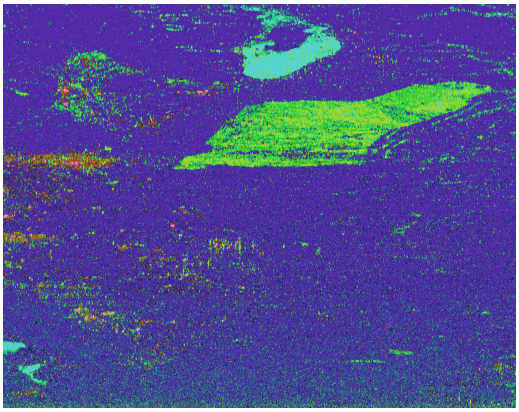

(c)Position and ensemble variation (proposed)

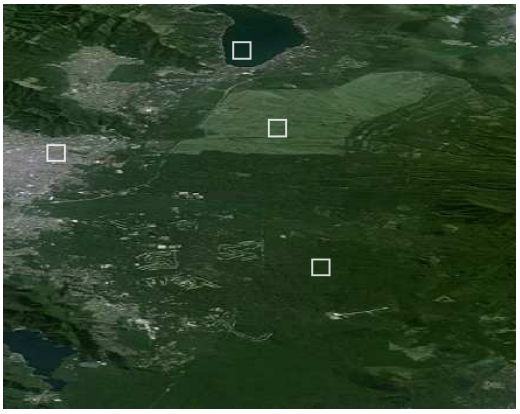

(d) Google photo

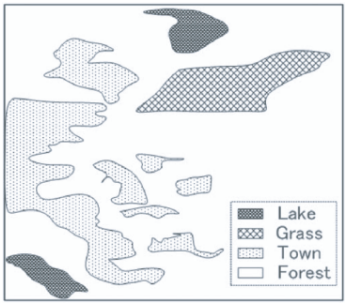

(e) Sketch into rough four classes shown in [27]

Figure 4: Land classification results for SOM with (a)position vector only, (b)position vector and spatial variation vector and (c)position vector and ensemble variation vector (proposal), as well as (d)Google optical photo with white squares indicating evaluation areas, and (e)a sketch showing four rough classes after [27].

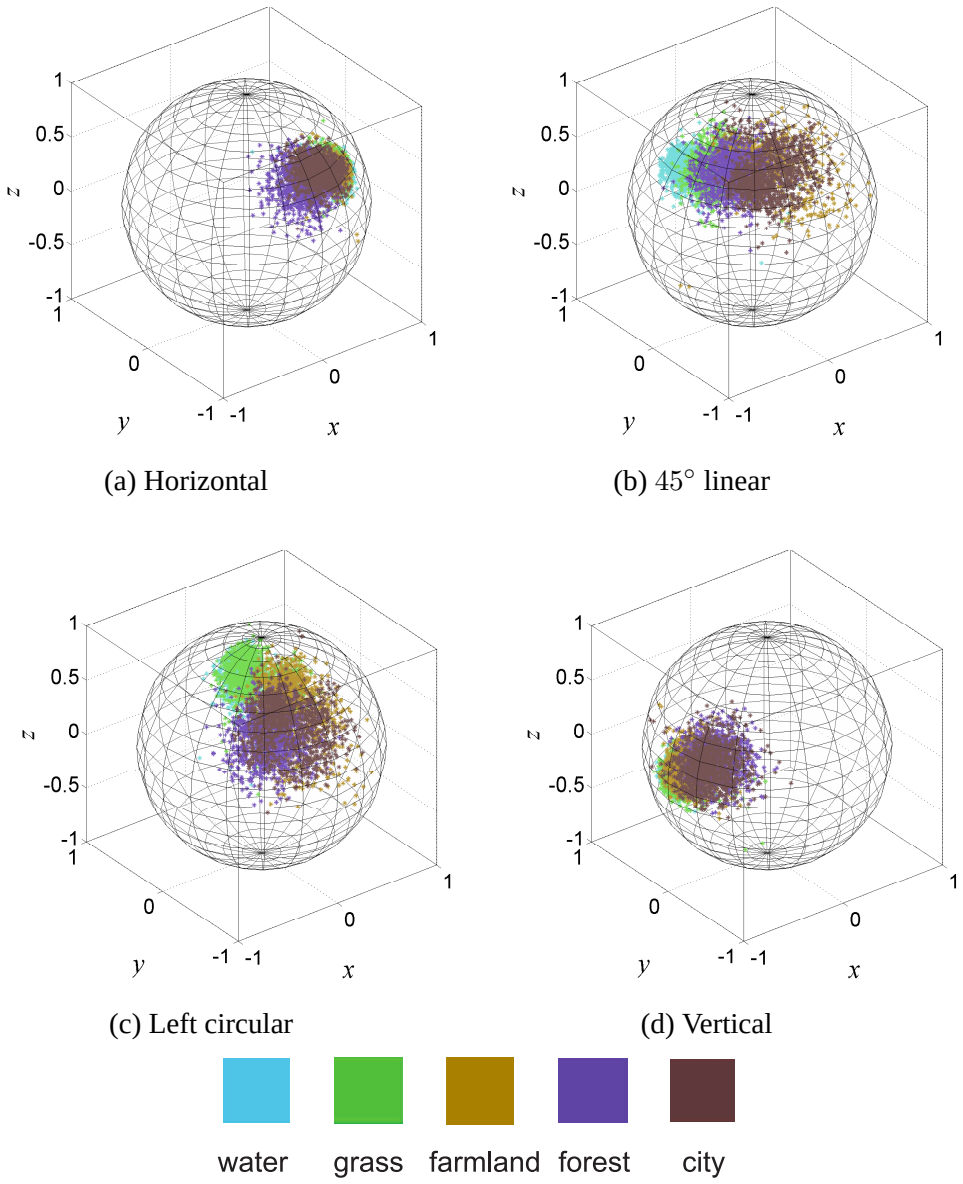

(a) Horizontal (b) 45° linear

(c) Left circular (d) Vertical

Figure 5: Position vectors of scattered wave for four polarization states of incident wave, namely, (a)horizontal, (b)45° linear, (c)left circular and (d)vertical polarizations.

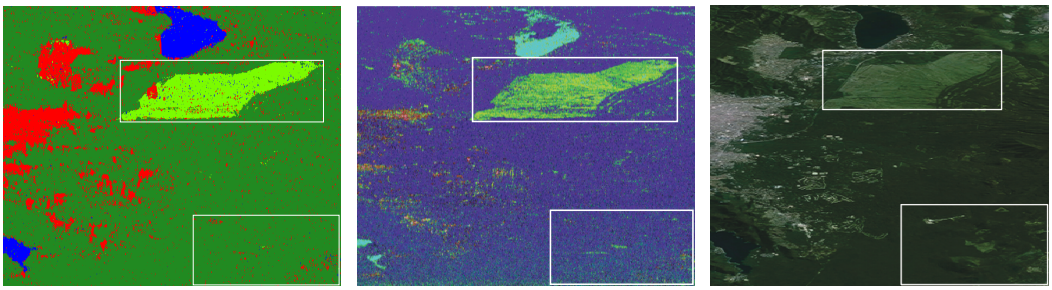

(a) Supervised result in [27] (b) Unsupervised result (proposal) (c) Google photo

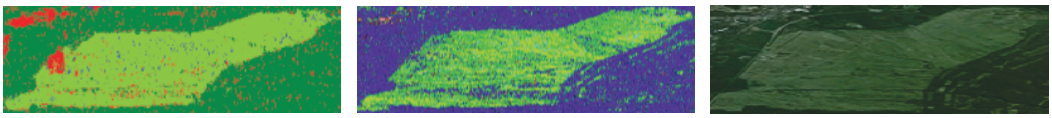

(a1) Close-up of field in (a) (b1) Close-up of field in (b) (c1) Close-up of field in (c)

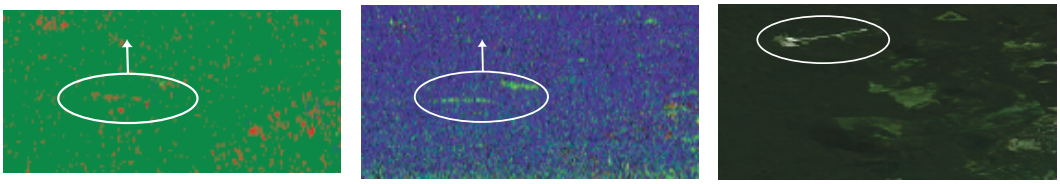

(a2) Close-up of forest in (a) (b2) Close-up of forest in (b) (c2) Close-up of forest in (c)

Figure 6: (a)Result of supervised learning in quaternion neural network [27], (b)result of the proposed unsupervised double-stage learning and (c)Google photo as well as close-up views for (a1)-(c1) the big grass field and (a2)-(c2) a ski gelaende in a mountainous area, resulting in foreshortening phenomenon in the SAR data. The required location compensation is indicated by the arrows in (a2) and (b2).

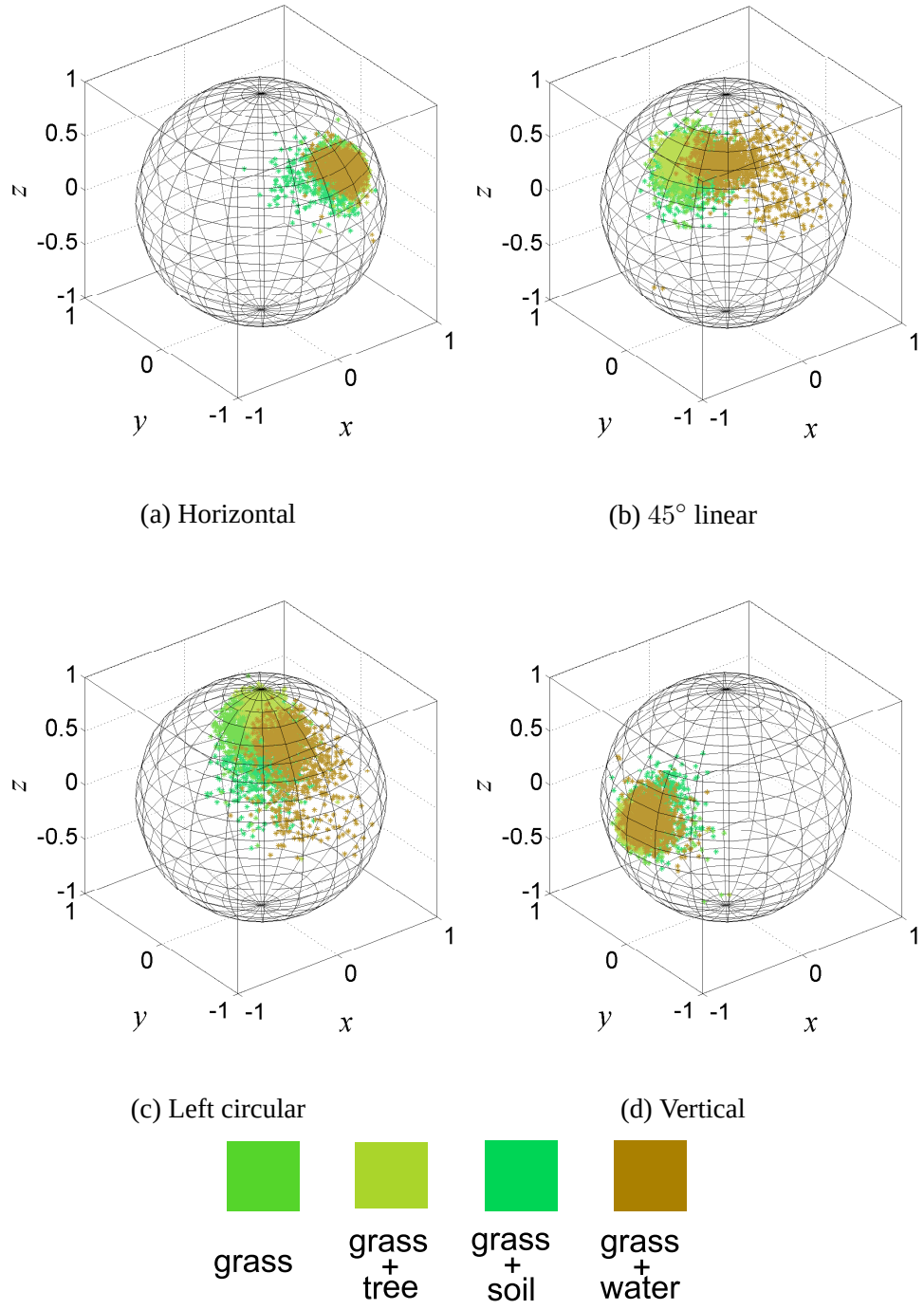

(a) Horizontal

(b) 45° linear

(c) Left circular

(d) Vertical

Figure 7: Position vectors of scattered wave showing fine classes for four polarization states of incident wave, namely, (a)horizontal, (b)45° linear, (c)left circular and (d)vertical polarizations.